

Magnetic and Optical Field Multi-Assisted Li-O₂ Batteries with Self-Regulated Charge and Discharge

Xiao-Xue Wang

Jilin University

De-Hui Guan

Jilin University

Fei Li

Jilin University

Ma-Lin Li

Jilin University

Li-Jun Zheng

Jilin University

Ji-Jing Xu (✉ jjingxu@jlu.edu.cn)

Jilin University <https://orcid.org/0000-0002-6212-8224>

Article

Keywords: Li-O₂ batteries, multi-assisted, self-regulated, 3D porous photoelectrode, ultra-low polarization

Posted Date: September 16th, 2020

DOI: <https://doi.org/10.21203/rs.3.rs-65969/v1>

License:   This work is licensed under a Creative Commons Attribution 4.0 International License.

[Read Full License](#)

Abstract

The photo-assisted lithium-oxygen (Li-O₂) system emerged as an important direction for future development by effectively reducing the large overpotential in Li-O₂ batteries. However, the advancement is greatly hindered by the rapidly recombined photoexcited electrons and holes upon the discharging and charging processes. Herein, we make a breakthrough in overcoming these challenges by developing a new magnetic and optical field multi-assisted Li-O₂ battery with 3D porous NiO nanosheets on the Ni foam (NiO/FNi) as a photoelectrode. Under illumination, the photogenerated electrons and holes of the NiO/FNi photoelectrode play a key role in reducing the overpotential during discharging and charging, respectively. By introducing the external magnetic field, the Lorentz force acts oppositely on the photogenerated electrons and holes, suppressing the recombination of charge carriers. The magnetic and optical field multi-assisted Li-O₂ battery achieves an ultra-low charge potential of 2.73 V, a high energy efficiency of 96.7%, as well as a good cycling stability of 200 h. This external magnetic and optical field multi-assisted technology paves a new way of developing high-performance Li-O₂ batteries and other energy storage systems.

Introduction

Rechargeable Li-O₂ batteries have aroused ever-increasing research interest in high-energy-density storage systems because of their high theoretical specific energy of 3500 Wh kg⁻¹ 1-4. However, the large overpotential of the batteries caused by sluggish ORR and OER kinetics (oxygen reduction and evolution reaction) is still a critical challenge to be surmounted (Fig. 1a) 5-6. To well resolve the aforementioned obstacles, a variety of strategies have been introduced, including the construction of electrocatalyst materials and soluble redox mediators 7-9. Although the charging voltage has been significantly reduced, electrocatalysts materials would expedite the parasitic decomposition of electrolyte during charging 10-11. Furthermore, soluble redox mediators migrate to the anode for reduction by electron shuttle, leading to low efficiency and instability of Li metal anode 12-13. Therefore, it is necessary to explore new ways to intrinsically promote the formation and decomposition of Li₂O₂ and reduce the large overpotentials of Li-O₂ battery.

Recently, incorporating green and renewable solar energy to improve the reaction kinetics of ORR and OER in Li-O₂ battery is recognized as one of the promising options (Fig. 1b) 14-16. Wu et al. first reported a photo-assisted Li-O₂ battery with the dye-sensitized TiO₂ photoelectrode, which efficiently utilize the photovoltage to scavenge the Li₂O₂ product 17. Zhou et al. further employed a graphitic carbon nitride (g-C₃N₄) as a cathode, achieving an ultra-low charge potential (1.96V) 18. However, the rapid recombination rate of the photoelectrons and holes generated in semiconductors is still a key obstacle in the photocatalyst-involved Li-O₂ battery. Conventionally, various state-of-art semiconductor heterojunctions, such as Schottky junctions, p-n junctions, and z-scheme heterostructures have been constructed to suppress the recombination of charge carriers 19-22. Yet, the synthetic methods for heterostructures are

complicated and rigorous. Accordingly, the noncontact and environmental-friendly external-magnetic-field-tuned approach can be used as an efficient strategy²³. It has been reported that the application of the magnetic field in the solar cell shows a significantly improved carrier separation and photoelectron conversion efficiency, which is ascribed to a deviation of the charge movement with a vertical force to the direction of movement in the magnetic field plane²⁴. Hence, it is feasible and significant to apply an external-magnetic-field into a photo-assisted Li-O₂ battery to enhance ORR and OER kinetics of the battery.

Based on the above understanding, we first report a novel prototype of magnetic and optical field multi-assisted Li-O₂ battery with a 3D porous NiO/FNi photoelectrode (Fig. 1c). Benefited from the abundant electron-hole pairs generated in the photoelectrode under the optical field, the difficult formation/decomposition of Li₂O₂ during the discharge/charge process in conventional Li-O₂ battery is greatly accelerated. When a magnetic field (MF) was introduced into the photo-assisted Li-O₂ battery system, the Li-O₂ battery could work stably at ultra-low Li₂O₂ oxidization voltage, which is ascribed to the well-suppressed electrons and holes. Notably, the charge voltage of the battery has achieved an ultra-low charge voltage ~2.73 V and a high stable cycling performance. Further tests were performed to discuss the interactions of the built-in electric fields, magnetic field and light, and its effects on the battery performance enhancement. The concept of the magnetic and optical field multi-assisted Li-O₂ battery offers an effective strategy to store the solar energy and introduces a universal method in energy storage systems.

Results

Structural analysis of the NiO/FNi cathode. Porous NiO nanosheets were in-situ deposited on the Ni foam (NiO/FNi) and employed as a photoelectrode in the magnetic and optical field multi-assisted Li-O₂ battery. The schematic diagram of the synthesis strategy for the NiO/FNi cathode is shown in Fig. 2a, which involves two steps, i.e., hydrothermal treatment and subsequent annealing at high temperature²⁵. The powder X-ray diffraction (PXRD) patterns of the final products are shown in Fig. 2b and all the diffractions are well indexed to cubic NiO. The X-ray photoelectron spectroscopy (XPS) further confirms the composition of the NiO/FNi cathode. In Fig. 2c, the peak located at 531.3 eV is assigned to the O of NiO-based material, and the peak at 532.7 eV is ascribed to the defective O. The peaks appear at 853.8 and 861 eV are attributed to the Ni 2p_{3/2} main peak and its satellite, and the 872.8 and 879.5 eV corresponded to Ni 2p_{1/2} main peak and its satellite (Fig. 2d)²⁶. The energy dispersive spectrum (EDS) element mappings reveal that the Ni and O atoms distribute uniformly across the NiO/FNi cathode (Supplementary Fig. 1). The microstructure of NiO/FNi cathode is investigated by the scanning electron microscopy (SEM, Fig. 2e), which displays the dense NiO nanosheets grown on Ni foam (Supplementary Fig. 2 and 3), as well as the color change from light to dark is displayed (inset). The enlarged SEM image of the NiO/FNi cathode clearly shows the homogeneously aligned and highly porous structure on a large scale (Fig. 2f). It is believed that the interconnected nanosheets can not only provide abundant open

space and electroactive surface for electron transfer and electrolyte diffusion, but also enough area for light adsorption. Transmission electron microscopy (TEM) image in low-magnification demonstrates the mesoporous structure of the NiO nanosheets, which can maximize the active surface and enable the achievement of excellent battery performance (Fig. 2g). The high resolution-TEM (HR-TEM) image shows a lattice fringe spacing distance of 0.148 nm, consistent with the (220) planes of face-centered cubic NiO, which is also in consistency with the NiO composition from the PXRD pattern²⁷. Furthermore, the nitrogen absorption-desorption isotherms suggest the interconnected porous structure with a high specific area of 144.77 m² g⁻¹ (Fig. 2h). Utilizing the advantages of maintaining good FNi macropores, NiO/FNi cathode could provide a low-resistance pathway for electron and mass transfer via the free-standing structure.

Photoelectrochemical behavior of NiO/FNi. The optical properties of NiO/FNi photoelectrode were investigated with a conventional three-electrode cell. The Mott-Schottky plots of NiO/FNi show a negative slope, which is typical for p-type semiconductors (Fig. 3a), indicating that the photo-induced holes are the dominant charge carriers. As can be seen from the ultraviolet-visible (UV-vis) absorption spectroscopy, the maximum absorption wavelength of NiO/FNi is about 410 nm (Fig. 3b) and the bandgap is further determined to be 3.12 eV by measuring the x-axis intercept from the Tauc plot (Supplementary Fig. 4)²⁸. The inset of Fig. 3b schematically shows that the CB and VB positions of NiO/FNi (vs. normal hydrogen electrode (NHE)). When NiO/FNi is excited by photons, electrons and holes can be transferred through the suitable positions, thus corroborating the potential of NiO/FNi as an efficient photoelectrode for the consequent ORR and OER processes. To evaluate the illumination effect on the photoelectrochemical ORR and OER process, liner sweep voltammetry (LSV) was detected in O₂-saturated 0.5 M Na₂SO₄ solution. The onset potential of NiO/FNi with illumination for ORR reaches up to -0.28 V vs. Ag/AgCl, suggesting that the effectively improved ORR catalytic performance is originated from the light (Fig. 3c). The photo-assisted ORR process on NiO/FNi is further confirmed by its current responses in Ar atmosphere with and without illumination in Supplementary Fig. 5. To better understand the reaction kinetics of the ORR process, Tafel slopes were calculated based on the LSV curves. The lower Tafel slope of 510 mV dec⁻¹ for NiO/FNi under light indicates that illumination plays a significant role in promoting the reaction kinetics of ORR (Fig. 3d). Additionally, during the OER process, the NiO/FNi under light also exhibits obviously favorable performance comparing to that in dark (Fig. 3e), demonstrating the positive effect of light during OER process. The smaller Tafel slope of NiO/FNi under light (259 mV dec⁻¹) than that in dark (429 mV dec⁻¹) further verifies the positive role on OER process (Fig. 3f). As shown in Supplementary Fig. 6, the EIS results show the reduced charge-transfer resistance of NiO/FNi under light compared to the initial electrode, leading to an increased conductivity, which is also consistent with the above results.

Photocatalytic properties of NiO/FNi under magnetic field. According to the previous work, Lorentz force can effectively act on photocatalysis process, due to the external MF can produce opposite force on the photoelectrons and holes^{19,21}. Thus, we applied NiO/FNi in the photocatalysis process with MF and without MF (MF and NMF, respectively) to understand the influence of MF on the photocatalytic activities.

Firstly, the nearly unchanged Mott-Schottky slopes of NiO/FNi under MF (Fig. 4a) imply that the MF has a slight influence on the intrinsic charge carrier density. The LSV curves for ORR at MF and NMF condition nearly show the same trend, suggesting that the Lorentz force cannot facilitate the photocatalytic process without the charge carriers generated via photoelectric conversion (Fig. 4b). Fig. 4c displays the photocatalytic ORR performance of the NiO/FNi under the MF and NMF conditions by using the magnetic photocatalyst setup (inset). The photogenerated current density obviously increased, suggesting that the presence of magnetic field plays a key role in enhancing the photocatalytic performance. In the presence of the external MF, electrons move under the function of the Lorentz force. Besides, driven by the Lorentz force, the free electrons in the system form a polarized distribution that generates a motion-induced electromotive force, which is probably the key reason for the enhancement of the photocatalytic performance. I-t curves were recorded under NMF and MF conditions to analyze the recombination rate of the charge carriers (Fig. 4d). The most stable and highest photocurrent response of the NiO/FNi under light and MF can be assigned to the newly separated photo-charges under MF conditions, which is related to the electromagnetic induction current.

To deeply understand the interaction between the photoelectrode and the magnetic field, the magnetic hysteresis loop (M-H) of NiO/FNi was measured at room temperature. As observed in Fig. 4e, M-H curve exhibits a typical ferromagnetic property with small coercivity and saturated under a magnetic field of 10 KOe, indicating NiO/FNi can be manipulated by an external magnetic field. According to the above experiment results, it is proposed that the electrons and holes can be deviated when they move in MF, leading to better separation of the charge carriers. The generated induced electromotive force under MF can interact with the photogenerated carriers through the mutual attraction of positive and negative charges, contributing to favorable charge separation. The schematic diagram clarified the influence of the MF on the NiO nanostructure under light (Fig. 4f). Herein, COMSOL was further performed to schematically illustrate the influence of the magnetic field on the NiO/FNi (Fig. 4g). Comparing with the Lorentz force of $\vec{F} = q(\vec{V} \times \vec{B})$ with the electric force of $\vec{F}_E = \vec{E}q$, the effects of the magnetic field on the charge carriers can be discussed by referring to the electric field¹⁹. It can be clearly seen that a parallel and homogenous electric field presented in the NiO nanosheets (NSs) based on the electromagnetic induction (Fig. 4h). Under magnetic field, the Lorentz force acts on the photo-induced electrons and holes due to the induced current difference between two sides, driving them to opposite directions, thus improving their efficient spatial separation and inhibiting recombination.

Electrochemical performance of the optical field assisted Li-O₂ battery. Applying NiO/FNi as the reversible photocathode, an optical field assisted Li-O₂ battery was constructed to investigate the effect of solar energy on the batteries (Fig. 5a). Due to the conversion of light energy to electricity, light-emitting devices can display higher brightness under illumination. Fig. 5b shows the galvanostatic charge and discharge curves of Li-O₂ battery with NiO/FNi, the illumination increases the discharge potential (from 2.59 V to 2.69 V) and concurrently decreases the charge potential (from 3.74 V to 2.92 V). Meanwhile, the optical field assisted Li-O₂ battery displays promoted energy efficiency from 69.3% to 92.1%, indicating the

positive effect of light on both the input and output electric energy conversion. On the one hand, the photogenerated electrons and holes on the surface of NiO/FNi in the optical field can act on the discharging and charging processes, respectively. On the other hand, the deposition and morphology of the discharge products could be adjusted in the optical field²⁹. The discharge products obtained in the dark densely coated on the nanosheets structure, which would hinder the contact between the electrolyte and the active sites, leading to large polarization during the subsequent charging process (Supplementary Fig. 7a). In sharp contrast, the film-like product deposited on the surface of the cathode in the optical field, which can maintain the active sites after the discharge process and are beneficial for the decomposition process (Supplementary Fig. 7b). Whether under dark or light, the discharge product Li₂O₂ was mostly decomposed after the 1st recharged (Supplementary Fig. 7c, d). However, the undecomposed Li₂O₂ accumulated on the cathode surface in the dark after 20th recharged, while the smooth cathode surface is still exposed in the optical field (Supplementary Fig. 8). These results suggesting that the reversible decomposition of Li₂O₂ was more effective in the optical field.

When suffering the periodic ON-OFF cycles, the Li-O₂ battery under light exhibits reproducible and continuous photo-responsiveness during the discharge and charge processes (Fig. 5c). The results suggest that the quick photoexcitation process and fast mass transfer under light could suppress the polarization of the battery. Moreover, the optical field assisted Li-O₂ battery presents better rate capability than that in dark (Supplementary Fig. 9). The voltage gaps between charge and discharge process are maintained within 1.85 V even at high current density of 1.2 mA cm⁻² and recovered to 0.36 V when returned to 0.01 mA cm⁻² after 40 cycles at different current densities, which further implying the facilitated effect of illumination on the rate capability (Supplementary Fig. 10). The oxygen reduction reaction (ORR) curves on the rotating disk electrode show improved kinetics under light, which is responsible for the excellent catalytic performance (Fig. 5d). The photoelectric conversion effect of NiO/FNi mainly acts on reducing the charging voltage and increasing discharge voltage upon illumination, which is corresponding to the position of CB and VB of NiO/FNi (Fig. 5e). During discharge, O₂ is reduced on the NiO/FNi surface involving the electron participation, thereby promoting the ORR. Under illumination, the photoelectrons from NiO/FNi transfer to the Li anode through the external circuit and hence reduce the Li⁺ to Li metals during charging. Meanwhile, holes can be collected on the NiO/FNi surface, and then utilized to oxidize the discharge product. Thus, the charge potential of NiO/FNi can be compensated by the generated photoelectric potential. In short, light plays a key role in achieving the energy storage and conversion from light to electrochemistry.

Electrochemical performance of the magnetic and optical field multi-assisted Li-O₂ battery. Inspired by the efficient effect of MF on photocatalysis, a magnetic and optical multi-assisted Li-O₂ battery was fabricated with NiO/FNi to study the influence of MF on the photoelectrochemical properties in the batteries. Fig. 6a depicted the charge potential of the battery under optical field and MF with different conditions. Notably, the charge potential of the battery was reduced to 2.73 V for the magnetic induction intensities of 5 mT, indicating that the existence of a permanent MF plays a significant role in enhancing the energy efficiency of the battery. Herein, the optimal magnetic induction intensity is selected to

evaluate of the magnetic and optical multi-assisted Li-O₂ battery performance. The first discharge and charge profiles of the magnetic and optical multi-assisted Li-O₂ battery with NiO/FNi at 0.01 mA cm⁻² under MF (5 mT) exhibited an ultra-low polarization voltage of ~ 0.09 V and a high energy efficiency of 96.7% (Supplementary Fig. 11). These results implied that more photogenerated electron-hole pairs existed in the batteries because the rapid recombination of the photo-carriers can be greatly hindered under the MF condition. Even at high current density of 1.2 mA cm⁻², the Li-O₂ battery under MF (5 mT) and light also shows the expected low charge voltage, which can be recovered to 2.78 V when returned to 0.01 mA cm⁻² after 40 cycles at different current densities (Fig. 6b). To further understand how MF facilitate the ion diffusion and improve the battery kinetics, EIS of photo-assisted Li-O₂ battery with NiO/FNi under MF was measured (Fig. 6c). The Nyquist plot of NiO/FNi MF (5 mT) light displays a much larger gradient, indicating a faster diffusion rate compared with NiO/FNi MF (0 mT) light. On the basis of the Nyquist plots³⁰, the Li⁺ diffusion coefficients' ratio of NiO/FNi MF light and NiO/FNi NMF light is determined to be 5:1, demonstrating a superior kinetics under MF for Li⁺ diffusion.

The Li-O₂ battery still shows stable discharge and charge platform without the increase in polarization after 120 h, which is attributed to the fact that the photo-induced electrons and holes can be separated in a long time under MF (Fig. 6d). The influence of the MF on the photo-assisted Li-O₂ battery is proposed and illustrated in Fig. 6d (inset). For a typical NiO/FNi photoelectrode, photogenerated electron-hole pair can easily recombine because the formed excited state obeys the conservation laws for energy and momentum, which results in limited participation of the photogenerated carriers in the charge transport. A potential or force to drive the positive and negative carriers towards opposite directions would significantly enhance the charge carrier density. MF was present during the photoelectrochemical process, according to the left-hand rule, both the moving electrons and holes experience a Lorentz force vertical to the direction of movement. Moreover, the forces acting on the negative electron and positive hole of the electron-hole pair are in opposite directions, leading to the deviation of the electrons and holes in opposite directions. Therefore, the photo-induced electron-hole pairs in moving semiconductor particles can be separated in MF, even at the initial generation of an electron-hole pair.

To further examine the stability of the magnetic and optical multi-assisted Li-O₂ battery upon cycling, the morphology changes of the recharged O₂ cathodes after the 30th cycle were examined. SEM image was carried out to investigate the discharge products under MF (5 mT) and light. The film-like morphology is similar to that under MF (0 mT) and light, indicating that MF has negligible effect on the morphology of the discharge products (Supplementary Fig. 12). The discharge product is evidenced by the Li 1s signal at 54.7 eV in the XPS spectra of NiO/FNi under MF (0 mT) and MF (5 mT) light, which reveals that Li₂O₂ is the only discharge product after the 30th discharged (Supplementary Fig. 13). After the 30th recharged, XRD patterns demonstrate that the Li₂O₂ can be oxidized completely during the charging progress (Fig. 6e). As shown in the SEM image, partial residues are still remained on the cathode after the 30th recharge under MF (0 mT) and light (Fig. 6f). This continuous accumulation of the undecomposed products upon cycling would hinder the transportation of the oxygen, electrons and lithium ions within the cathode

during subsequent cycling. In sharp contrast, the film-like discharge products have disappeared, and the homogeneously nanosheets structure of the whole cathode is almost fully recovered, even after the 30th recharge under MF (5 mT) and light, implying good structure reversibility and stability of the magnetic and optical multi-assisted Li-O₂ battery (Fig. 6g). The Li 1s signal at 54.7 eV in the XPS spectra of NiO/FNi further reveals the reversible Li₂O₂ decomposition under MF (0 mT and 5 mT) light after the 30th recharged (Fig. 6h). Moreover, gas chromatography was performed on the batteries to demonstrate the gas evolution on recharge. As shown in Supplementary Fig. 14, the results imply that O₂ are detected as the predominant gas over the recharge process. Tiny amounts of CO₂ gas (μL) are traced in the battery under light and magnetic field, suggesting the positive effect of the external field on the decomposition of Li₂O₂. All the above-mentioned results support that the optical and magnetic field play an active and important role in enhancing the Li-O₂ battery performance.

Discussion

In summary, we have introduced the magnetic field into the photo-assisted Li-O₂ battery system for the first time to improve its ORR and OER kinetics. It is revealed that under illumination, the photogenerated electrons and holes can significantly act on the charging and discharging process, respectively. The photogenerated electrons participate in promoting the reduction of O₂ during the discharging process, while the generated holes favor the oxidization of Li₂O₂ upon charging. The interactions of the built-in electric fields, magnetic field and light, and its effects on the battery performance enhancement were studied in detail. Taking advantage of the magnetic field, the efficient effect of light illumination is prolonged owing to strong inhibition effects on the rapid recombination of the charge carriers. Herein, NiO/FNi is served as the all-in-one bifunctional photocathode combining magnetic effect and photoelectric conversion function, which endows effective modulation of internal electric properties, transportation of electrons and Li ions and redox reactions in the batteries. Importantly, the battery under light and magnetic field delivers an ultra-low charge voltage of 2.73 V, a high energy efficiency of 96.7%, and a good cycling stability of 200 h. This conceptual work provides a general and effective paradigm in the development of high-performance energy devices with the effect of magnetic field and other external fields.

Methods

Synthesis of NiO/FNi photocathode. All the reagents were of analytical grade and used as received. In a typical synthesis procedure, Ni foam (2.5×2.5 cm) was first pretreated in a HCl (6 M) for 10 min to remove the surface NiO layer, and then cleaned with deionized water and ethanol for 5 min. The obtained sample was then transferred into a Teflon-lined stainless-steel autoclave with a solution (50 mL) containing Ni(NO₃)₂·6H₂O (0.582 g, 2 mmol), NH₄F (0.148 g, 4 mmol) and CO(NH₂)₂ (0.601 g, 10 mmol), maintained at 105°C for 5 h, then cooled down to room temperature. The samples were collected, thoroughly washed with distilled water, and dried. Finally, the obtained sample was calcined in air at 350 °C for 2 h to obtain

the mesoporous NiO nanosheet arrays on Ni foam. The loading density of the NiO on the Ni foam was calculated to be 2 mg cm^{-2} .

Material characterization. The crystallographic information and chemical composition of the as-prepared products were established by a Rigaku D-Max 2550 diffractometer using Cu K α radiation. The morphological investigations were carried out on a JEOL JSM-6700F scanning electron microscope. Microstructures were characterized by high-resolution transmission electron microscopy (HRTEM, a JEM-2200FS electron microscope). Nitrogen adsorption–desorption isotherms were measured at 77 K with a Micromeritics 2020 analyzer. The specific surface area was calculated with the Brunauer-Emmett-Teller (BET) equation, and the pore size distribution was calculated from the adsorption curve by the Barrett-Joyner-Halenda (BJH) method. X-ray photoelectron spectroscopy (XPS) was recorded on an ESCALAB 250 spectrometer. The UV-vis spectra were acquired with a U-4100 UV-vis spectrometer under the diffuse-reflection model using an integrating sphere (UV 2401/2, Shimadzu). The fluorescence spectra of the samples were taken by the photoluminescence (PL) spectrofluorometer (FLUOROMAX-4 spectrophotometer) with an excitation at 300 nm light. The magnetic properties of the samples were measured using a vibrating sample magnetometry (SQUID-VSM magnetic measurement system, USA).

Electrochemical measurements. The electrochemical tests were performed on a CHI 660E electrochemical workstation at room temperature in a three-electrode configuration. A platinum plate and Ag/AgCl were used as the counter electrode and reference electrode, respectively. Freshly prepared Na_2SO_4 (0.5 M) aqueous solution was used as the electrolyte. Electrochemical impedance spectroscopy (EIS) was conducted in the frequency range between 100 kHz and 0.01 Hz. The ORR and OER performance of the NiO/FNi cathode were analyzed through the LSV via rotating disk electrode (RDE) technique in O_2 -saturated 0.5 M Na_2SO_4 and LITFSI/DME. The galvanostatic discharge-charge cycling tests were performed on Land-CT2001A battery-testing system (Wuhan LAND electronic Co. Ltd, China) with and without illumination, respectively.

Declarations

Data availability

The data supporting the findings of this study are available within the paper and its Supplementary Information, and from the corresponding author upon reasonable request.

Acknowledgements

This work was financially supported by the National Natural Science Foundation of China (Grant 51771177, 51972141, 21621001, 21835002), the 111 Project (B17020), the Education Department of Jilin Province (JJKH20190113KJ), Jilin Province Science and Technology Development Program (20190303104SF), the Jilin Province/Jilin University Co-construction Project-Funds for New Materials (SXGJSF2017-3).

Author contributions

J.J.X. and X.X.W. developed the concept, designed the experiments, and co-wrote the manuscript. X.X.W prepared materials, performed the experimental measurements and experimental data analysis. All authors discussed the results and commented on the manuscript.

Competing financial interests

The authors declare no competing interests.

Additional information

Supplementary information is available in the online version of the paper. Reprints and permission information is available online at <http://www.nature.com/reprints>. Correspondence and requests for materials should be addressed to J.J.X.

References

1. T. Liu, J. P. Vivek, E. W. Zhao, J. Lei, N. Garcia-Araez, C. P. Grey, Current Challenges and Routes Forward for Nonaqueous Lithium-Air Batteries. *Chem. Rev.* **120**, 6558-6625 (2020).
2. P. Zhang, Y. Zhao, X. B. Zhang, Functional and stability orientation synthesis of materials and structures in aprotic Li-O₂ batteries. *Chem. Soc. Rev.* **47**, 2921-3004 (2018).
3. P. Wang, C. X. Li, S. H. Dong, X. L. Ge, P. Zhang, X. G. Miao, R. T. Wang, Z. W. Zhang, L. W. Yin, Hierarchical NiCo₂S₄@NiO Core-Shell Heterostructures as Catalytic Cathode for Long-Life Li-O₂ Batteries. *Adv. Energy Mater.* **9**, 1900788 (2019).
4. P. Wang, C. X. Li, S. H. Dong, X. L. Ge, P. Zhang, X. G. Miao, Z. W. Zhang, C. X. Wang, L. W. Yin, One-Step Route Synthesized Co₂P/Ru/N-Doped Carbon Nanotube Hybrids as Bifunctional Electrocatalysts for High-Performance Li-O₂ Batteries. *Small* **15**, 1900001 (2019).
5. M. Balaish, X. W. Gao, P. G. Bruce, Y. Ein-Eli, Enhanced Li-O₂ Battery Performance in a Binary "Liquid Teflon" and Dual Redox Mediators. *Adv. Mater. Technol.* **4**, 1800645 (2019).
6. K. Baek, W. C. Jeon, S. Woo, J. C. Kim, J. G. Lee, K. An, S. K. Kwak, S. J. Kang, Synergistic effect of quinary molten salts and ruthenium catalyst for high-power-density lithium-carbon dioxide cell. *Nat. Commun.* **11**, 456 (2020).
7. Z. M. Huang, H. P. Zeng, M. L. Xie, X. Lin, Z. M. Huang, Y. Shen, Y. H. Huang, A Stable Lithium-Oxygen Battery Electrolyte Based on Fully Methylated Cyclic Ether. *Angew. Chem. Int. Ed.* **131**, 2367-2371 (2019).
8. Y. H. Chen, S. A. Freunberger, Z. Q. Peng, O. Fontaine, P. G. Bruce, Charging a Li-O₂ battery using a redox mediator. *Nat. Chem.* **5**, 489-494 (2013).
9. Y. Q. Chang, S. M. Dong, Y. H. Ju, D. D. Xiao, X. H. Zhou, L. X. Zhang, X. Chen, C. Q. Shang, L. Gu, Z. Q. Peng, G. L. Cui, A Carbon- and Binder-Free Nanostructured Cathode for High-Performance

- Nonaqueous Li-O₂ Battery. *Adv. Sci.* **2**, 1500092 (2015).
10. Q. Peng, S. A. Freunberger, Y. H. Chen, P. G. Bruce, A Reversible and Higher-Rate Li-O₂ Battery. *Science* **337**, 5 (2012).
 11. X. H. Yao, Q. Dong, Q. M. Cheng, D. W. Wang, Why Do Lithium–Oxygen Batteries Fail: Parasitic Chemical Reactions and Their Synergistic Effect. *Angew. Chem. Int. Ed.* **55**, 11344-11353 (2012).
 12. H. Kim, W.-J. Kwak, H.-G. Jung, Y.-K. Sun, Verification for trihalide ions as redox mediators in Li-O₂ batteries. *Energy Storage Mater.* **19**, 148-153 (2019).
 13. W.-H. Ryu, F. S. Gittleston, J. M. Thomsen, J. Y. Li, M. J. Schwab, G. W. Brudvig, A. D. Taylor, Heme biomolecule as redox mediator and oxygen shuttle for efficient charging of lithium-oxygen batteries. *Nat. Commun.* **7**, 12925 (2016).
 14. Z. Zhu, X. M. Shi, G. L. Fan, F. J. Li, J. Chen, Photo-energy conversion and storage in an aprotic Li-O₂ battery. *Angew. Chem. Int. Ed.* **58**, 19021-19026 (2019).
 15. D. D. Zhu, Q. C. Zhao, G. L. Fan, S. Zhao, L. B. Wang, F. J. Li, J. Chen, Photo-Induced Oxygen Reduction Reaction Boosts The Output Voltage of Zn-Air Battery. *Angew. Chem. Int. Ed.* **58**, 12460-12464 (2019).
 16. X. R. Liu, Y. F. Yuan, J. Liu, B. Liu, X. Chen, J. Ding, X. P. Han, Y. D. Deng, C. Zhong, W. B. Hu, Utilizing solar energy to improve the oxygen evolution reaction kinetics in zinc–air battery. *Nat. Commun.* **10**, 4767 (2019).
 17. M. Z. Yu, X. D. Ren, L. Ma, Y. Y. Wu, Integrating a redox-coupled dye-sensitized photoelectrode into a lithium–oxygen battery for photoassisted charging. *Nat. Commun.* **5**, 5111 (2014).
 18. Y. Liu, N. Li, S. C. Wu, K. M. Liao, K. Zhu, J. Yi, H. S. Zhou, Reducing the charging voltage of a Li-O₂ battery to 1.9 V by incorporating a photocatalyst. *Energy Environ. Sci.* **8**, 2664-2667 (2015).
 19. W. Gao, J. Lu, S. Zhang, X. Zhang, Z. Wang, W. Qin, J. Wang, W. Zhou, H. Liu, Y. Sang, Suppressing Photoinduced Charge Recombination via the Lorentz Force in a Photocatalytic System. *Adv. Sci.* **6**, 1901244 (2019).
 20. Q. Li, J. Fu, W. Zhu, Z. Chen, B. Shen, L. Wu, Z. Xi, T. Wang, G. Lu, J. J. Zhu, S. Sun, Tuning Sn-Catalysis for Electrochemical Reduction of CO₂ to CO via the Core/Shell Cu/SnO₂ Structure. *J. Am. Chem. Soc.* **139**, 4290-4293 (2019).
 21. J. Li, S. K. Cushing, P. Zheng, T. Senty, F. Meng, A. D. Bristow, A. Manivannan, N. Wu, Hydrogen Generation by a CdS-Au-TiO₂ Sandwich Nanorod Array Enhanced with Au Nanoparticle as Electron Relay and Plasmonic Photosensitizer. *J. Am. Chem. Soc.* **136**, 8438-8449 (2014).
 22. J. Ran, M. Jaroniec, S. Z. Qiao, Solar Cocatalysts in Semiconductor-based Photocatalytic CO₂ Reduction: Achievements, Challenges, and Opportunities. *Adv. Mater.* **30**, 1704649 (2018).
 23. J. Li, Q. Pei, R. Wang, Y. Zhou, Z. Zhang, Q. Cao, D. Wang, W. Mi, Y. Du, Enhanced Photocatalytic Performance through Magnetic Field Boosting Carrier Transport. *ACS Nano* **12**, 3351-3359 (2018).
 24. W. Gao, Q. Liu, S. Zhang, Y. Yang, X. Zhang, H. Zhao, W. Qin, W. Zhou, X. Wang, H. Liu, Y. Sang, Electromagnetic induction derived micro-electric potential in metal-semiconductor core-shell hybrid

- nanostructure enhancing charge separation for high performance photocatalysis. *Nano Energy* **71**, 104624 (2020).
25. Z. Lin, C. Du, B. Yan, C. Wang, G. Yang, Two-dimensional amorphous NiO as a plasmonic photocatalyst for solar H₂ evolution. *Nat. Commun.* **9**, 4036 (2018).
26. S. Tong, M. Zheng, Y. Lu, Z. Lin, J. Li, X. Zhang, Y. Shi, P. He, H. Zhou, Mesoporous NiO single-crystalline utilized as noble metal-free catalyst for non-aqueous Li-O₂ battery. *J. Mater. Chem. A* **3**, 16177-16182 (2015).
27. H. Wang, Y. Xia, H. Li, X. Wang, Y. Yu, X. Jiao, D. Chen, Highly active deficient ternary sulfide photoanode for photoelectrochemical water splitting. *Nat. Commun.* **11**, 3078 (2020).
28. J. Liu, Y. Liu, N. Liu, Y. Han, X. Zhang, H. Huang, Yeshayahu Lifshitz, Shuit-Tong Lee, J. Zhong, Z. Kang, Metal-free efficient photocatalyst for stable visible water splitting via a two-electron pathway. *Science* **347**, 970-974 (2015).
29. Y. Feng, H. Xue, T. Wang, H. Gong, B. Gao, W. Xia, C. Jiang, J. Li, X. Huang, J. He, Enhanced Li₂O₂ Decomposition in Rechargeable Li-O₂ Battery by Incorporating WO₃ Nanowire Array Photocatalyst. *ACS Sustainable Chem. Eng.* **7**, 5931-5939 (2019).
30. D. H. Guan, X. X. Wang, M. L. Li, F. Li, L. J. Zheng, X. L. Huang, and J. J. Xu, Light/Electricity Energy Conversion and Storage for a Hierarchical Porous In₂S₃@CNT/SS Cathode towards a Flexible Li-CO₂ Battery. *Angew. Chem. Int. Ed.* **59**, 2-9 (2020).

Figures

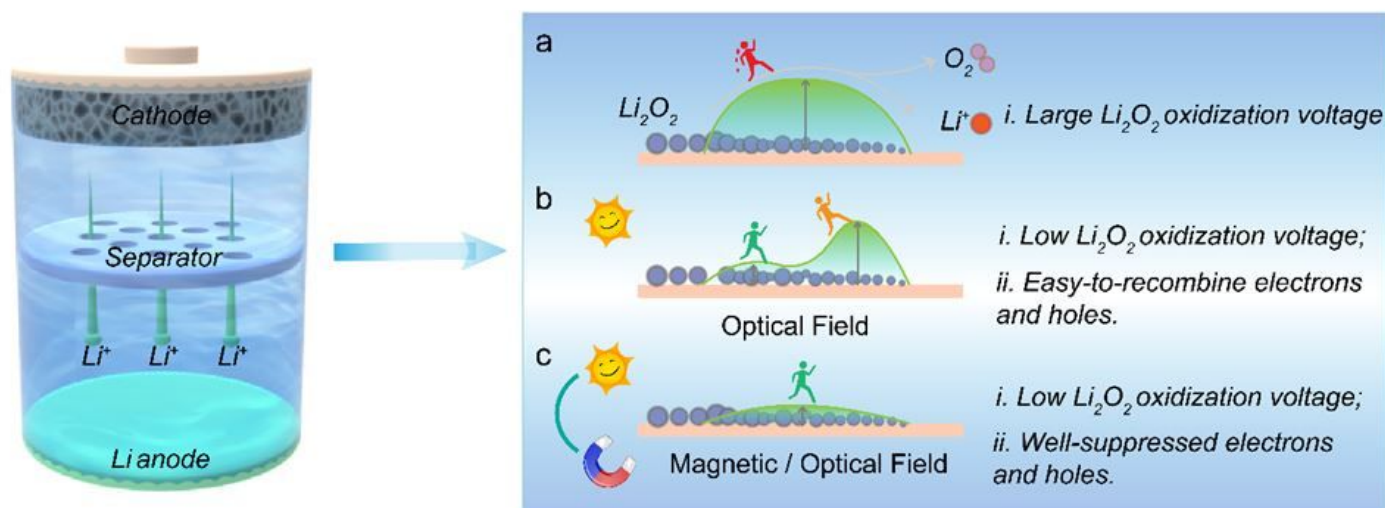


Figure 1

Working schematic illustration of Li-O₂ batteries (left part) at different environments. The diagram shows the decomposition of the discharge products during the charging process (right part). The working

mechanism of Li-O₂ battery is based on electrochemical reaction, $2\text{Li} + \text{O}_2 \rightleftharpoons \text{Li}_2\text{O}_2$ ($E = 2.96 \text{ V}$, vs Li^+/Li).

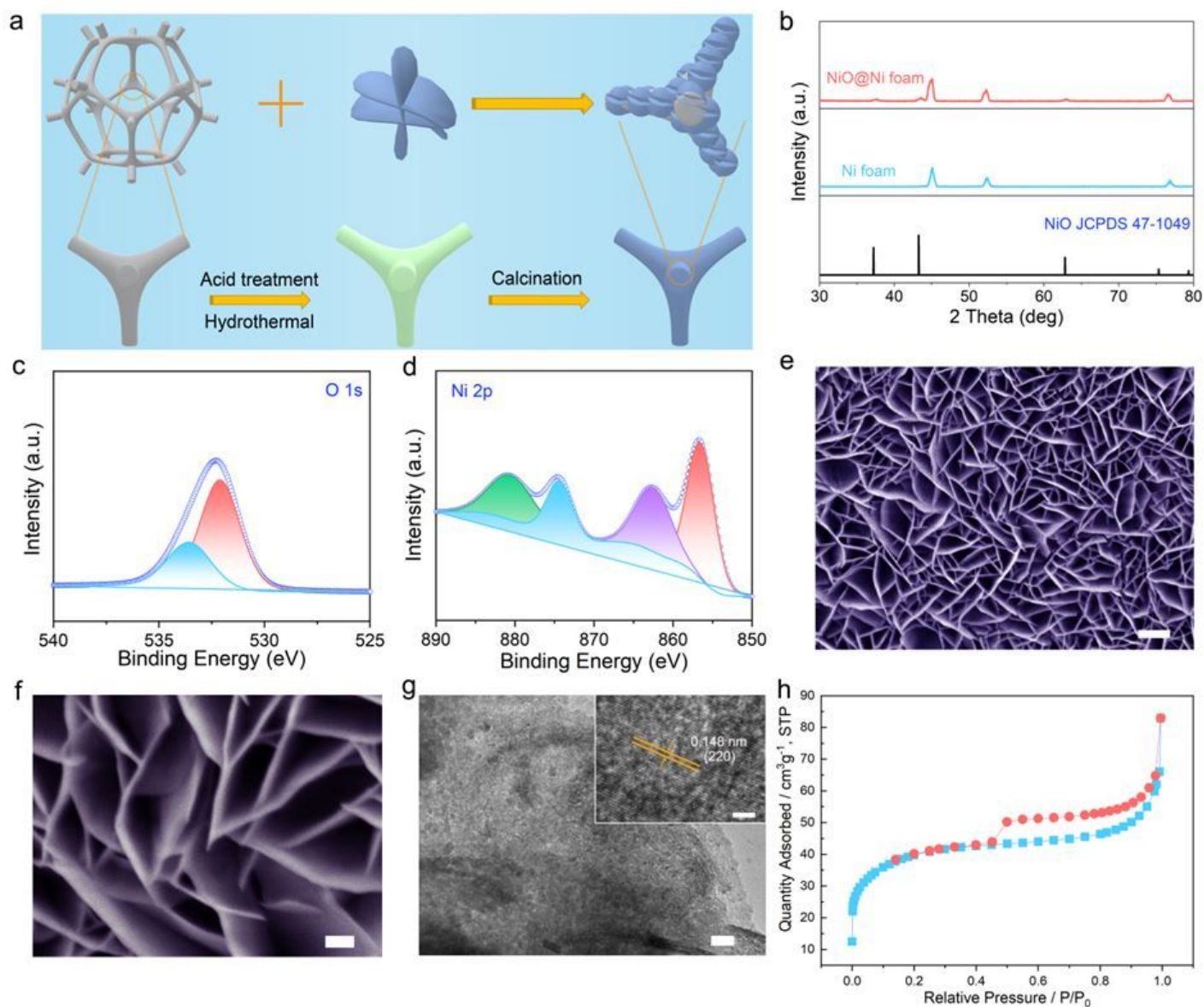


Figure 2

Structure of the NiO/FNi cathode. a The synthesis schematic diagram of the NiO/FNi cathode. b The powder X-ray diffraction (PXRD) patterns of the NiO/FNi cathode. c, d High-resolution O 1s and Ni 2p XPS spectrum of NiO/FNi cathode. e, f The SEM images of the NiO/FNi cathode with different magnifications. Scale bars in e, f are 1 μm and 200 nm. g TEM and HRTEM images of NiO/FNi cathode. Scale bars in g and inset are 20 nm and 2 nm. h N₂ adsorption and desorption isotherm of the NiO/FNi cathode.

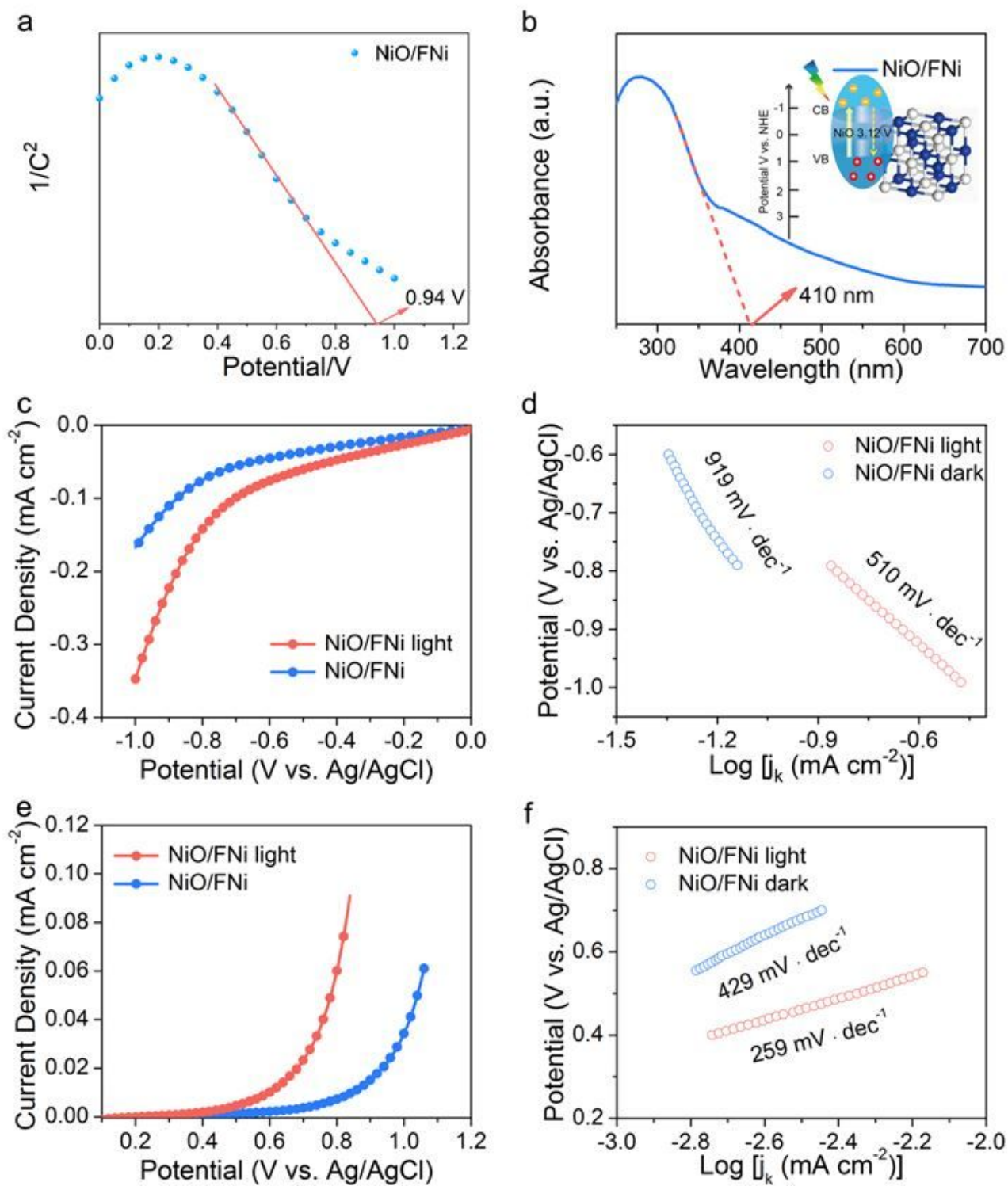


Figure 3

Photoelectrochemical behavior of NiO/FNi. a Mott-Schottky plots of NiO/FNi. b UV-Vis spectrum of NiO/FNi. Inset is the schematic diagram of energy levels for NiO/FNi. c LSV curves of ORR at 5 mV s^{-1} . d Corresponding Tafel curves. e LSV curves of OER at 5 mV s^{-1} . f Corresponding Tafel curves.

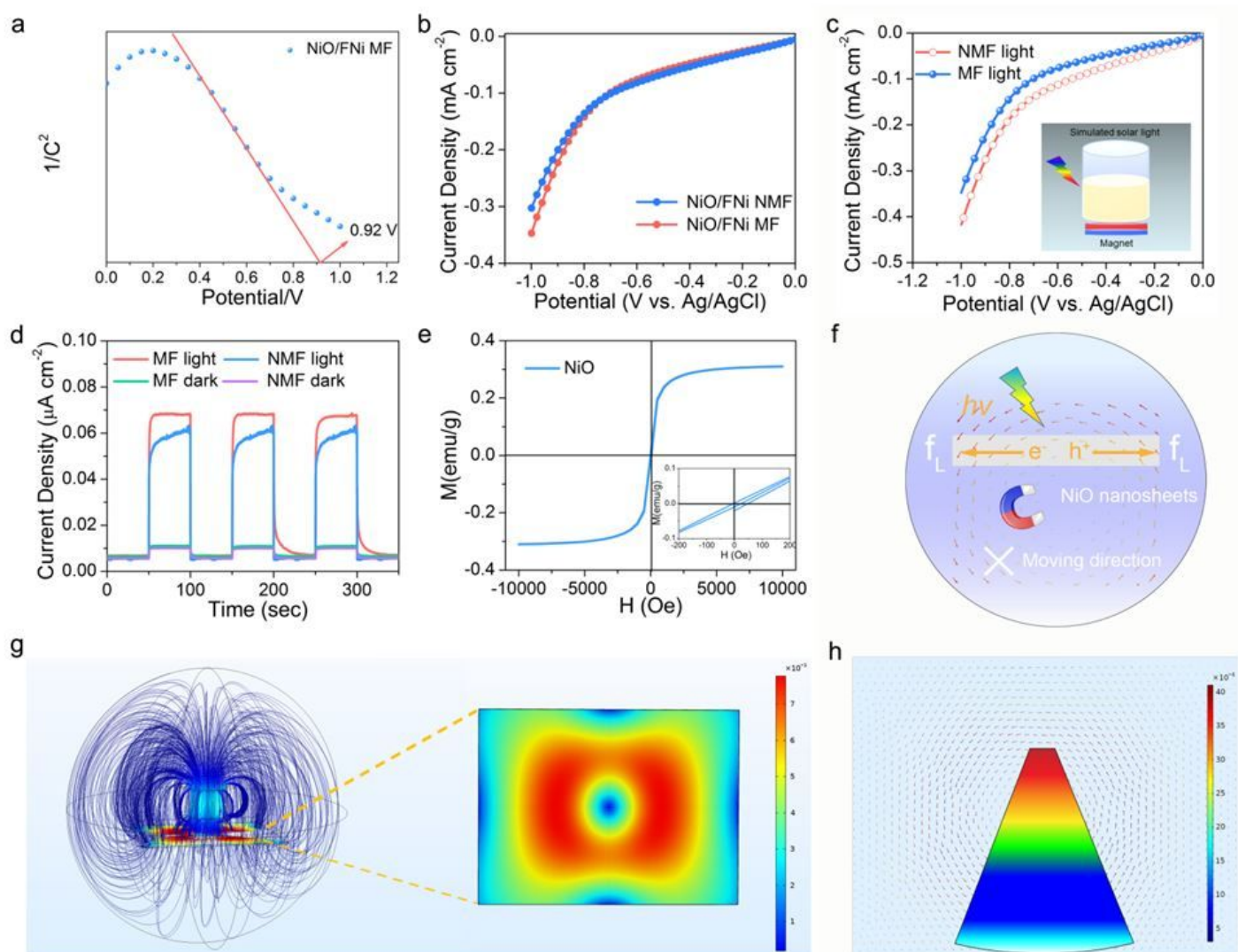


Figure 4

Photocatalytic properties of NiO/FNi under magnetic field. a Mott-Schottky plots of NiO/FNi under MF condition. b LSV curves for ORR in O₂-saturated 0.5 M Na₂SO₄ solution under NMF and MF conditions. c LSV curves for ORR in O₂-saturated 0.5 M Na₂SO₄ solution under NMF and MF conditions with light. d I-t curves of the NiO/FNi under NMF and MF conditions. e Magnetic hysteresis loop for NiO/FNi at room temperature. Inset: magnified views of the low-field region. f Schematic diagram of the interaction between the magnetic field and the NiO nanosheets under illumination. g-h Induced electromotive force of NiO, a schematic diagram of the relative motion between the magnetic field and the NiO, and COMSOL simulated distribution of surface-induced electromotive force of NiO under MF.

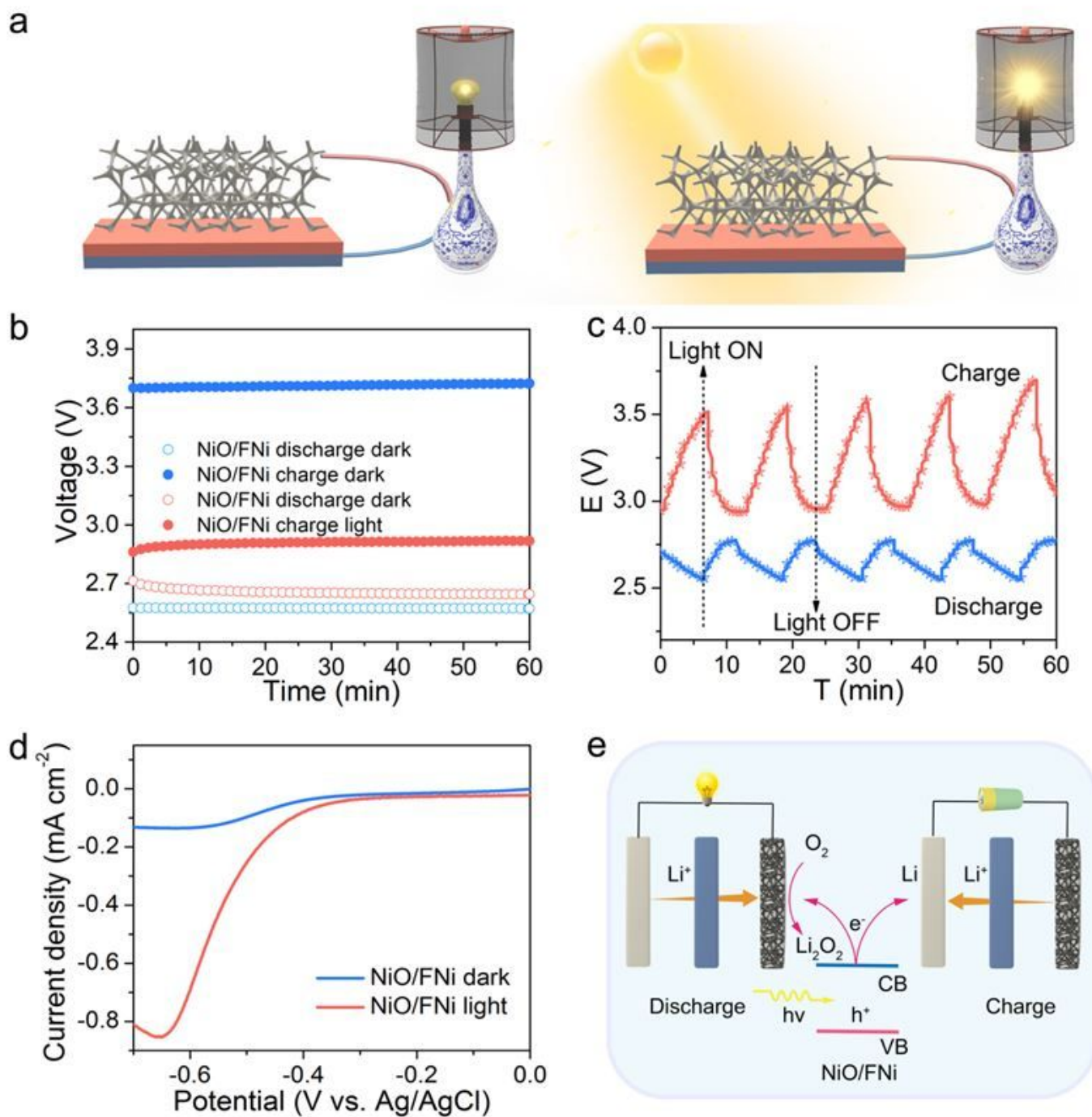


Figure 5

a Structure and working principle of NiO/FNi under light. b Galvanostatic charge/discharge curves of NiO/FNi in the dark and under light. c Solar-light-responsive charge/discharge curves of NiO/FNi in the dark and under light. d LSV curves measured in ORR region of NiO/FNi with and without illumination in O_2 -saturated 0.5 M of LiTFSI/DME solution at a scan rate 5 mV s^{-1} . The rotating speed was 1600 rpm. e Working principle of the solar light-responsive NiO/FNi.

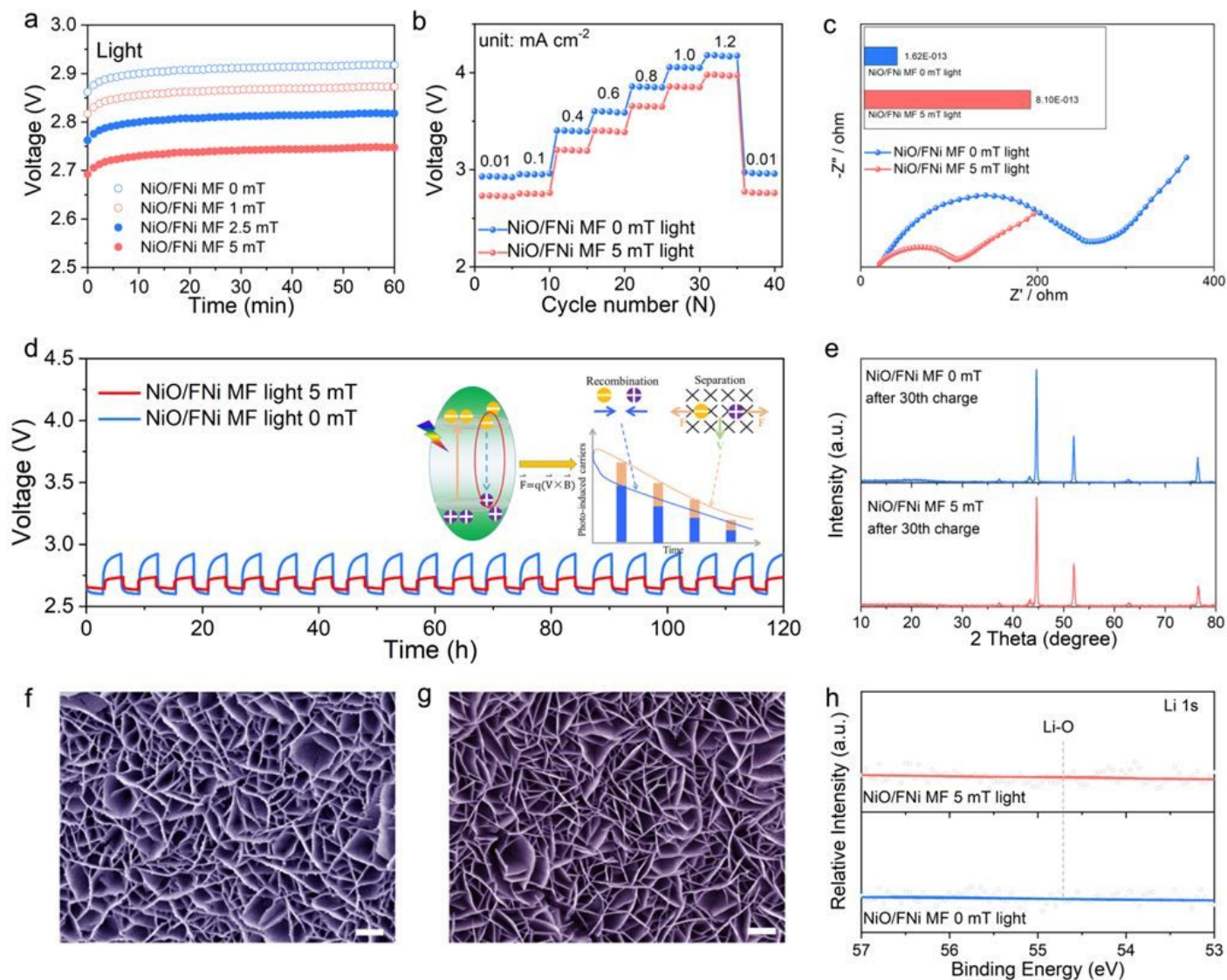


Figure 6

a The charge potential of the battery under optical field and MF at different current densities. b Charge voltage variation of Li-O₂ batteries under optical field and MF (0 mT and 5 mT). c Electrochemical impedance spectra (EIS) of Li-O₂ batteries under optical field and MF (0 mT and 5 mT). Inset is the calculated Li⁺ diffusion coefficient. d The voltage profiles of typical Li-O₂ batteries cycled with 0.01 mAh cm⁻² cut-off capacity under optical field and MF (0 mT and 5 mT). Inset is the schematic diagram of magnetic and optical field multi-assisted process. e XRD patterns of the 30th recharged cathodes under optical field and MF (0 mT and 5 mT). f, g The SEM images of the 30th recharged cathodes under optical field and MF (0 mT and 5 mT). Scale bars in f, g are 1 μm. h Li 1s XPS spectrum of the 30th recharged cathodes under optical field and MF of (0 mT and 5 mT).

Supplementary Files

This is a list of supplementary files associated with this preprint. Click to download.

- [SupportingInformation.docx](#)
- [TableofContents.docx](#)